Article

Insights into the Gelation Mechanism of Metal-Coordinated Hydrogels by Paramagnetic NMR Spectroscopy and Molecular Dynamics

Valeria Gabrielli, Roberto Baretta, Roberto Pilot, Alberta Ferrarini, and Marco Frasconi*

Cite This: *Macromolecules* 2022, 55, 450−461

Read Online

ACCESS | Metrics & More | Article Recommendations | SI Supporting Information

ABSTRACT: Metal-coordination complexes are attracting increasing attention as supramolecular cross-linkers to develop polymeric hydrogel networks with tunable and dynamic mechanical properties. Nonetheless, the rational design of these materials is still hindered by the limited mechanistic understanding of how metal−ligand interactions influence the structure and properties of the hydrogel. Here, we report a detailed mechanistic investigation using nuclear magnetic resonance (NMR) spectroscopy combined with molecular dynamics (MD) simulations to explore the formation of cellulose-based hydrogels induced by coordination with paramagnetic Fe^{3+} ions. We demonstrate how NMR paramagnetic relaxation enhancement can be used to probe the distances between the metal center and NMR active nuclei on the polymer chain, informing on the metal−ligand coordination network. Experimental results, together with supporting MD simulations, allow us to uncover a structuration of water around the cross-linked metals within the hydrogel, in addition to the establishment of different orientations of the chains governed by hydrogen bonds networks. Progress in understanding the gelation mechanism of metal-coordinated hydrogels will fuel their exploitation for a wide variety of biomedical applications.
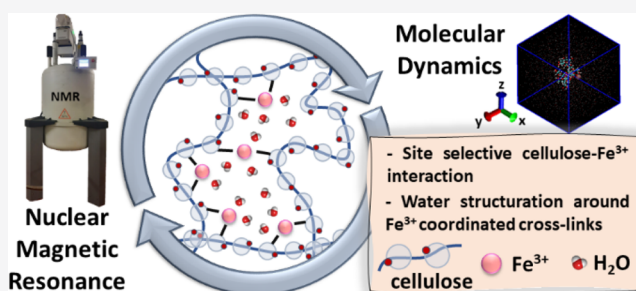
INTRODUCTION

Even though metal ions have been associated with biological systems for billions of years, scientists really appreciated the scale of their influence only in the last century. Biological systems, such as marine mussels that incorporate several ligands to form metal-coordinated bonds,[1] have inspired the use of transition metal-coordination complexes as cross-linkers of polymeric hydrogels to engineer their properties for a wide range of applications.[2−5]

Transition metals have empty orbitals in which they can locate a lone pair of electrons donated by a ligand and create a reversible dative chemical bond, generating a flexible connection between the ligand and the ion. Importantly, the capacity of metal-coordination bonds to reform after rupture enables the formulation of hydrogels with tunable, dynamic, stimuli-responsive, self-organizing, and self-healing mechanical properties.[1] Progress in developing metal-coordinated hydrogels with defined properties for a variety of applications, that are still being developed, depends critically on understanding the metal−ligand geometries of interactions and the related mechanism of gelation. For these systems, methods enabling a full characterization of the interaction between the coordinating ligands and the coordinated metals are in need for a deep understanding of the molecular mode of function.[2,6,7]

In this context, nuclear magnetic resonance (NMR) spectroscopy and molecular dynamics (MD) calculations have proven to be excellent tools to achieve a fundamental understanding and atomistic details of the mechanism of gelation, unraveling the dynamics and structure of the interacting constituents of the hydrogel, including the crucial role that water plays during gelation.[8−10] In addition, combination with other analytical techniques, such as vibrational and X-ray spectroscopies, is an effective strategy to achieve a multiscale view of metal-coordinated hydrogels, establishing a link between the hydrogel' chemical structure, the nature of metal-coordinated and cross-linked molecular structures, and the larger-scale organization.

Natural biopolymers, such as cellulose, are attracting increasing interest as alternatives to petroleum-based polymers due to their high availability and environment-friendly nature. Taking advantage of the complex interactions of such biopolymers with water, hydrogels derived from cellulose have been engineered for applications spanning from sensor interfaces to smart drug delivery and packaging and energy storage systems.[11]
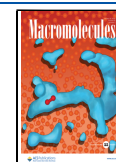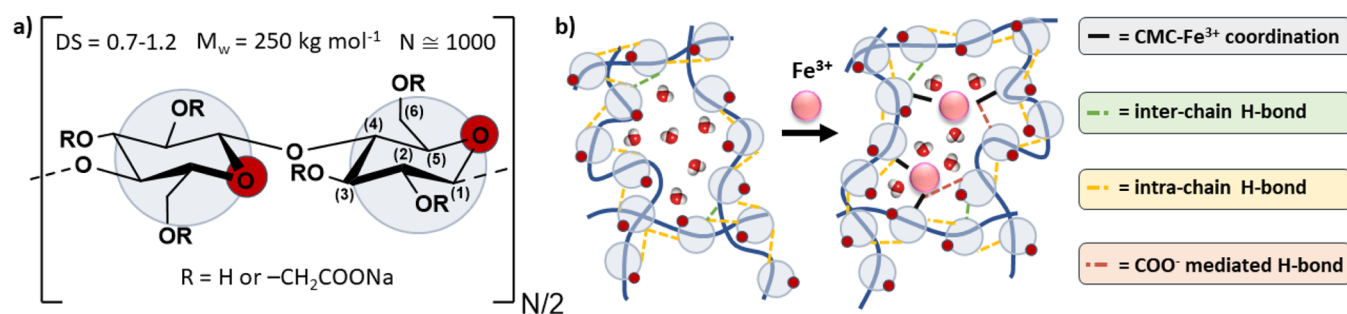
Scheme 1. (a) Chemical Structure of Cellobiosyl Units of CMC and Characteristics of CMCs Used in This Study; (b) Schematic Representation of the Questions Herein Addressed; How Do Added Fe^{3+} Ions Interact With the CMC Monomeric Units, Form Interchain Connections, and Induce Solvent Structuration Leading to the Formation of CMC–Fe^{3+} Hydrogel[a]

[a]CMC degree of polymerization ($N \approx 1000$) is determined from the ratio between the average M_w and the monomer weight ($M_m \sim 220$ g mol^{-1}). The numbers in brackets indicate the carbon position.

Among various cellulose derivatives, carboxymethyl cellulose (CMC) is largely used for applications in paper, textile, paint, food, and pharmaceutical industries due to its remarkable thickening, suspension, binding, and emulsifying functional properties.[12] Recently, CMC-based hydrogels have been evolving as promising bioinks and 3D/4D scaffold biomaterials with possible applications in regenerative medicine.[13] Due to its polyelectrolyte nature, CMC dispersion viscosity decreases with an increase in the salt concentration (decrease in the excluded volume and electrostatic stiffening).[14] For diluted solutions, the addition of multivalent and specifically coordinating ions can result in significant conformational changes in CMC chains.[15] In addition, the weak nature of the reversible ionic interactions between metal ions and CMC chains might donate temperature- and pH-responsive properties to the 3D gel network.[15]

One of the key features of CMC is its chelating property and the resulting ability to form 3D gel structures at a pH close to neutrality in the presence of bivalent[16] (i.e., Zn^{2+}) and trivalent[17] (i.e., Fe^{3+}) metal cations. In particular, iron cross-linking can be used to induce redox-controlled structural changes of the hydrogel promoted by the interconversion of Fe^{2+} and Fe^{3+} ions.[18,19] It has been reported, for example, that polysaccharides such as alginate [poly(guluronan-co-mannuronan)] or pectate [poly(galacturonan)] complexed with Fe^{3+} ions formed redox- and photo-responsive materials that are able to convert from hydrogels to sols under electrochemical potential[20] or irradiation with visible light.[21,22] In addition, the paramagnetic nature of Fe^{3+} cross-linked hydrogels can impart the ability to respond to magnetic fields. Recently, CMC–Fe^{3+} hydrogels formulated into cytocompatible double-network hydrogels have been proposed as scaffolds for tissue engineering applications.[23]

The physicochemical properties of CMC–Fe^{3+} gels are determined by the degree of substitution (DS) of the carboxymethyl groups on the cellulose chains and the nature and concentration of the iron salt used as the cross-linker. Oxo-bridges between the negatively charged carboxylate groups and the trivalent cations established via ionic interactions and coordination bonds have been described as the leading intermolecular contacts responsible for chain–chain association.[17] A tetrahedral coordination and a bidentate chelating mode were assigned to Fe^{3+} ions in a complex with CMC via Fourier transform infrared (FT-IR) characterization.[17] Yet, relatively little is known about the mechanisms of the mutable

metal-coordinated bonds occurring in CMC–Fe^{3+} hydrogels. Specifically, structural information about the complexes' formation and the influence of the metal ions on the polysaccharide structure and its interaction with water molecules are still missing.

Here, we present a novel approach for the structural characterization of supramolecular hydrogels coordinated by transition metals with paramagnetic nature. A combination of short-range (NMR, Raman, and FTIR spectroscopies) and long-range (powder X-ray diffraction (PXRD)) characterization techniques and molecular modeling calculations provides a detailed investigation on the gelation mechanism and the nature of the chemical interactions at the CMC–Fe^{3+} interface (Scheme 1). Specifically, the paramagnetic relaxation enhancement (PRE) induced by paramagnetic Fe^{3+} ions has allowed us to explore the proximity and selectivity of the interaction between the Fe^{3+} and the differently substituted carboxylate groups of CMC. Strikingly, our results unveiled a selective mode of binding in the formation of the CMC–Fe^{3+} hydrogel, showing that the presence of Fe^{3+} ions promotes intra-ring connection over inter-residue association in the initial stages of gelation. Our theoretical results agree almost perfectly with the experimental data, demonstrating, for the first time, a structuration of water around the coordinating Fe^{3+} ions in the hydrogel and the active role played by the carboxylate group that acts as a hydrogen-bond acceptor in interchain connections. The method that we developed here could also be extended to the mechanistic investigation of other metal-coordinated hydrogels, paving the way for the rational design of tunable materials from the most fundamental scale and up.

■ EXPERIMENTAL SECTION

Materials. Sodium CMC (NaCMC, average MW 250,000) with a DS of 0.7, 0.9, and 1.2 was purchased from Sigma-Aldrich. $Fe(NO_3)_3 \cdot 9H_2O$ (ACS reagent ≥98%) was purchased from Sigma-Aldrich. All reagents were purchased from commercial suppliers and used without further purification.

Sample Preparation. All salt-free NaCMC suspensions were prepared by dilution from a 2% w/v stock dispersion. The CMC–Fe^{3+} dispersions were prepared by adding on a 2% w/v dispersion of CMC a Fe^{3+} stock solution, to achieve the final desired concentrations. To avoid nucleation of the gel by addition of Fe^{3+} ions, the samples were kept under continuous stirring conditions.

Nuclear Magnetic Resonance. For the NMR experiments, two different sets of samples were prepared for each of the investigated DS of CMC: (i) a dispersion of CMC 1% w/v in D_2O and (ii) the

corresponding sample with 5 mM $Fe(NO_3)_3$. The maximum Fe^{3+} concentration of 5 mM was selected to maintain the sample in an "in the process of gelling" state.[24] Under those conditions, an acceptable resonance broadening is obtained for the viscous fluid "gel" state, allowing us to obtain qualitative indications of which nuclei are affected upon gelation. In addition, for CMC with a DS of 0.9, $Fe(NO_3)_3$ concentrations of 0.5, 0.75, and 1 mM were also tested. Before sample formulation, $Fe(NO_3)_3$ was solvent exchanged with deuterium oxide (D_2O—99.8% isotropic purity). Following this, all the samples were prepared in D_2O and placed in a 5 mm NMR glass tube (Wildman, USA) for a total volume of 600 μL. All NMR experiments were performed using a Bruker DMX 600 MHz cryoprobe spectrometer operating at 600.13 MHz for ^1H experiments and 150.90 MHz for ^{13}C experiments, equipped with a 5 mm room-temperature TXI probe. All spectra were acquired and processed with Bruker TopSpin version 4.1.1 on a Windows PC.

2D ^1H–^{13}C HSQC experiments were carried out for the characterization of the CMC 1% w/v dispersions, in the absence and in the presence of Fe^{3+} ions. Phase-sensitive 2D ^1H–^{13}C HSQC experiments were acquired *via* INEPT transfer using echo–antiecho and adiabatic pulses for inversion. The inter-pulse delay time was set to 3.44 ms, which correspond to 1/4 J_{CH}, and a total of 128 t1 acquisitions with 48 scans per increment were collected. In order to target the fast-relaxing components for CMC both in the absence and in the presence of Fe^{3+} ions, the experimental relaxation delay was set to 2 s. For CMC DS 0.9, Fe^{3+} titration experiments were performed for a final concentration of Fe^{3+} ions in solutions of 0.5, 0.75, 1, and 5 mM. For CMC with a DS of 0.7 and 1.2, exclusively the experiments with 5 mM Fe^{3+} were performed. In addition, HSQC experiments run with a relaxation delay of 21.5 s (five times the longest average T1 of CMC of 4.3 s) were acquired for CMC with a DS 0.7, 0.9, and 1.2 in the absence and in the presence of Fe^{3+} ions collecting 64 t1 acquisitions with 16 scans per increment. A semiquantitative analysis of the volume integrals of the HSQC correlation peaks was carried out. Importantly, to accurately evaluate the volume of correlation peaks, a manual integration was performed. The change in the volume of correlation peaks upon addition of Fe^{3+} ions was measured as the ratio of the absolute integrals of the samples in the presence (reduced volume) to those of the samples in the absence (full volume) of Fe^{3+} ions. HSQC spectra of CMC samples (DS 0.7, 0.9, and 1.2) in the absence and in the presence of 5 mM Fe^{3+} ions were run in triplicates. The integral ratio was measured using the average integrals from the three repetitions, and the error propagation for the integral ratio was calculated.

Saturation-transfer difference (STD) NMR experiments of CMC dispersions in the absence and in the presence of 5 mM Fe^{3+} were acquired at 298 K using a train of 50 ms Gaussian-shaped pulses for selective saturation of the gelator particles; on-resonance and off-resonance frequencies were set up to −1 (for selective saturation of the CMC network)[25] and 50 ppm, respectively. For CMC dispersion in the absence of Fe^{3+} ions, STD NMR experiments were performed using saturation times ranging from 1 to 20 s, with a constant time length per scan (saturation time + recycle delay) of 20 s. Depending on saturation time, STD NMR experiments were performed with 64 scans or less (with a minimum of eight scans), in inverse relation to the saturation time, and 4 dummy scans. For CMC dispersions in the presence of Fe^{3+} ions, experiments with saturation times ranging from 0.1 ms to 8 s were acquired. A constant time length per scan (saturation time + recycle delay) of 8 s was used. STD NMR experiments were performed with 256 scans or less (with a minimum of eight scans), in inverse relation to the saturation time, and 4 dummy scans.

Subtraction of the on- (I_{sat}) to the off-resonance (I_0) spectra resulted in the STD spectra (I_{STD}). Following this, the peak intensities of the I_{STD} difference spectrum were integrated relative to the peak intensities of the I_0 off-resonance spectrum to obtain the STD factor (η_{STD}).

For application of the Spin Diffusion Transfer Difference (SDTD) methodology,[10] the obtained STD factors were normalized against the highest value (corresponding to the longest saturation time). Thus,

the SDTD values were obtained and plotted against the square root of the saturation time ($t_{sat}^{1/2}$).

The obtained SDTD build-up curves were then fitted to the SDTD equation, derived from Fick's second law of diffusion[10]

$$\mathrm{SDTD} = C \cdot \mathrm{erfc}\left[\frac{r}{2 \cdot \sqrt{D_{SD} \cdot t_{sat}}} - b\right] \tag{1}$$

where SDTD is the normalized STD intensity values, C is the proportionality constant of the fit, erfc is the complementary error function, r is the minimum distance between the gelator particles and the HDO molecule (expressed in nm), D_{SD} is the spin diffusion coefficient at the particle–solvent interface (expressed in nm^2/ms), t_{sat} is saturation time (expressed in ms), and b is a correction factor to center the Gaussian distribution. Fitting of the curves was performed by keeping the r and b parameters constant. The r parameter was set to 2 Å, a value already reported for water–particle interfaces.[26] For the b parameter, several values were tested until the best fit was obtained. Importantly, the dependence of D_{SD} on the b value used during the fit determines that only D_{SD} values obtained from curve fits processed with the same b parameter can be compared.

Vibrational Spectroscopy. *Raman Spectroscopy.* The (home-built) Raman instrument is equipped with an Ar^+/Kr^+ gas laser (Coherent, Innova 70) operated at 514.5 nm. The laser beam is filtered through a tunable plasma line filter (Spectrolab, Laserspec III), coupled to a microscope (Olympus, BX41) and focused on the sample by a 20× objective (Olympus, LMPlan FLN 20× NA = 0.40). The back-scattered Raman signal is coupled into the slit of a three-stage subtractive spectrograph (Jobin Yvon S3000) by means of a set of achromatic lenses. The triple spectrograph is composed of a double monochromator (Jobin Yvon, DHR 320) that rejects the elastic scattering and a spectrograph (Jobin Yvon, HR 640). The Raman signal is detected by a liquid nitrogen-cooled CCD (Jobin Yvon, Symphony, 1024 × 256 pixels, front illuminated). The slit width was set at 100 μm. Spectra were recorded with a laser power at the sample from 0.5 to 5 mW; the integration time was set in between 10 and 20 s, and 20 to 40 acquisitions were averaged together. CMC (DS 0.9) 4% w/v and CMC 4% w/v with $Fe(NO_3)_3$ 50 mM dispersions in Milli-Q water were prepared. All the samples were analyzed after water remotion by evaporation (CMC 4% w/v) or freezer-drying [CMC 4% w/v with $Fe(NO_3)_3$ 50 mM].

Fourier-Transform Infrared Spectroscopy. FTIR spectra were obtained with an FT-IR Nicolet Nexus 670 spectrometer, and all samples were prepared as potassium bromide pellets. 25 scans were collected with a resolution of 2 cm^{-1}. CMC (DS 0.9) 4% w/v and CMC 4% w/v with $Fe(NO_3)_3$ 50 mM dispersions in Milli-Q water were prepared and then freezer-dried. All the samples were analyzed in powder form and after gentle grinding with a mortar and pestle.

Powder X-ray Diffraction. X-ray diffraction patterns were recorded on a Bruker D8 ADVANCE Plus diffractometer in Bragg–Brentano geometry employing Cu Kα line radiation, a motorized anti-scatter screen, and a LYNXEYE EX-T position-sensitive detector operating in the 1D mode. The patterns were acquired in the 5–40° 2θ range (0.05°/step and 2 s/step). 4% w/v CMC dispersions in Milli-Q water in the absence and in the presence of 50 mM $Fe(NO_3)_3$ were prepared and freezer-dried. All the samples were analyzed in powder form and after gentle grinding with a mortar and pestle.

MD Simulations. D-cellotriose-methylated derivatives were constructed using GLYCAM carbohydrate builder[27] and used as starting structures. The molecules were then converted into the corresponding carboxymethylated derivatives using Schrödinger (MAESTRO).[28] Subsequently, *tleap* (AmberTools20)[29] was used to construct the initial conformations for the trimer simulations using the carbohydrate-optimized GLYCAM06 force field.[30] The Fe^{3+} ion and Cl^- counter-ion were introduced in the system with the *addions* plug-in of AmberTools in *tleap* using the Li/Merz non-bonded interaction parameters for divalent to tetravalent ions for the TIP3P water model (12-6-4 set).[31] The coordination and topology files were then converted into the GROMACS format using *acpype*[32] and solvated in
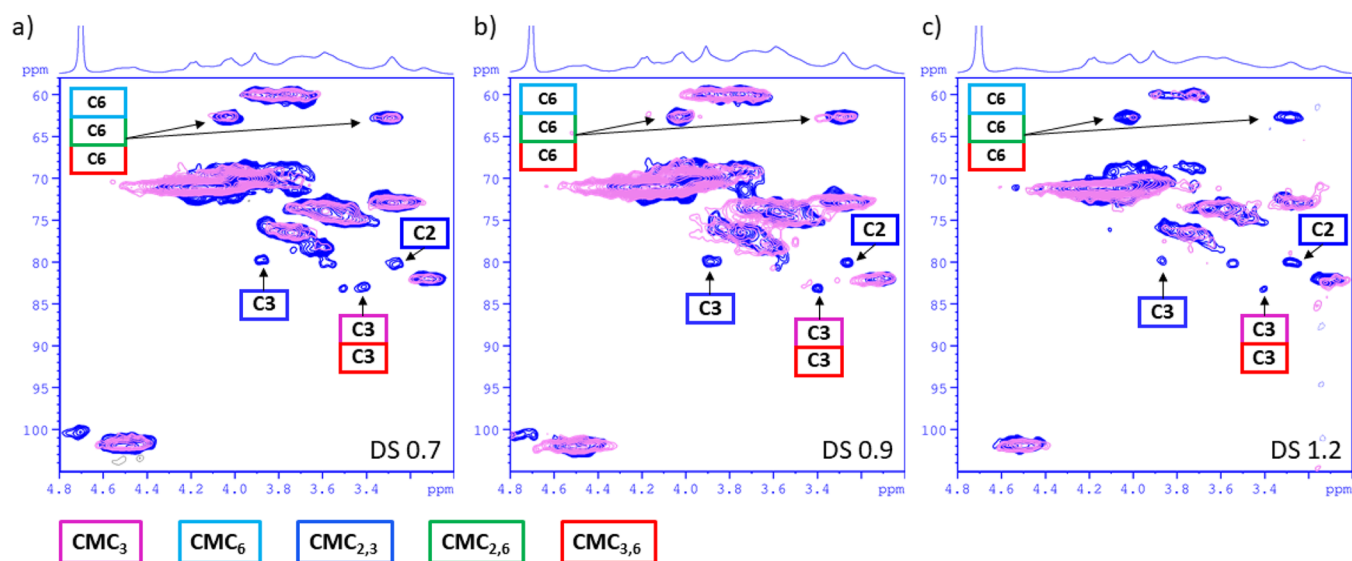
Figure 1. Superimposed 2D $^1H-^{13}C$ HSQC spectra of 1% w/v CMC dispersion with a DS of (a) 0.7, (b) 0.9, and (c) 1.2, recorded in the absence (blue) and in the presence (pink) of 5 mM Fe^{3+} in D_2O. In the spectra, the carbon position corresponding to each monomer is reported (*cf.* Scheme 1). Only the carbons showing the interaction with Fe^{3+} are labeled. In the legend, the subscript number indicates the position of the carboxymethyl substitution in the glucopyranose unit.

a cubic simulation box (4 nm × 4 nm × 4 nm) with 1000 TIP3P water molecules using GROMACS tools.

MD simulations were performed using GROMACS 2020.1.[33,34] A Nosé–Hoover thermostat and a Parrinello–Rahman barostat were used to keep the systems at a constant temperature of 303 K and at a constant pressure of 1 bar, respectively. A 1.4 nm cut-off was set for non-bonded interactions. The particle mesh Ewald method was used to calculate long-range electrostatics.[35] The LINCS algorithm[36] was applied to constrain bonds involving hydrogens. During all the MD simulations, a 2 fs time step was used. The simulations were carried out under periodic boundary conditions. After energy minimization (steepest descent algorithm), the systems were equilibrated for 20 ns at 303 K in a canonical (*NVT*) ensemble (constant number of particles, volume, and temperature) and subsequently for 20 ns at 303 K and 1 atm in an isothermal–isobaric (*NPT*) ensemble.

Simulations were carried out for three single-chain systems composed of carboxymethylated D-cellotriose with a double substitution introduced in the central ring (2′,3′-carboxymethyl cellotriose, 2′,6′-carboxymethyl cellotriose, and 3′,6′-carboxymethyl cellotriose) and for six double-chain systems composed of two chains of carboxymethylated D-cellotriose with a single substitution introduced at the central-ring level (2′-carboxymethyl cellotriose, 3′-carboxymethyl cellotriose, and 6′-carboxymethyl cellotriose). All systems were simulated for 100 ns, except for the systems containing 6′-carboxymethyl cellotriose which were simulated for 200 ns.

In order to prevent a "ring flip" artifact, a dihedral restraint using an equilibrium angle of −47° and a force constant of 20 20 20 [*x, y, z*; kJ/(mol rad²)] have been applied to the dihedral angle C1−C2−C3−C4 for the 2′,6′-carboxymethyl cellotriose and for the 3′-carboxymethyl cellotriose in 3′-mono/3′-mono and 3′-mono/6′mono systems.[37]

RESULTS AND DISCUSSION

Structural Bases of Fe^{3+}-Induced Gelation of CMC: An Atomistic Prospective. NMR spectroscopy is a well-known technique to investigate the structure and dynamics of complex systems, such as proteins or soft materials (*i.e.*, hydrogels),[38,39] and is one of the most powerful analytical methods for characterizing cellulose derivatives.[39] In the case of soft materials, such as cellulose, solution-state NMR experiments show only the magnetization arising from the more mobile part

of the sample, that is, the chain segments that are solvent-exposed.[39] Nonetheless, in ^1H NMR spectra, those signals can be broad and not well-resolved.[40] On the contrary, ^{13}C NMR spectra for swelled polymeric gels give rise to signals sufficiently resolved to obtain structural information.[41]

In the case of CMC hydrogels, the coexistence of eight different anhydroglucose units (AGUs), namely unsubstituted and the 2-mono, 3-mono, 6-mono, 2,3-di, 2,6-di, 3,6-di, and 2,3,6-trisubstituted AGUs, randomly distributed along the carbon chains of cellulose derivatives, results in complex ^1H and ^{13}C NMR spectra. In these spectra, signal overlapping hinders unambiguous chemical shift assignments. Nonetheless, Kono *et al.* were able to precisely assign ^{13}C chemical shifts of CMC with different DS by a combination of multiple 1D and 2D NMR approaches. For example, they recorded and assigned the 1D ^{13}C spectrum for ^{13}C-labeled CMC with a DS of 0.91.[42] In addition, they reported the HSQC and the TOCSY-HSQC spectra of CMC with a DS ranging from 0.68 to 2.84.[43] On these grounds, in deciphering CMC−Fe^{3+} interactions, we relied on 2D $^1H-^{13}C$ HSQC spectra which showed higher chemical shift dispersion and well-resolved unambiguous peaks compared with 1D ^1H spectra, together with an acquisition time of few hours in comparison to tens of hours or even days required for direct ^{13}C acquisition for unlabeled and diluted CMC dispersions.

The DS of CMC is defined as the number of CH_2-COO^- groups per AGU. In other words, the DS defines the number of three types of monomers (mono, di, or trisubstituted, represented by *m*, *n*, and *p*, respectively) in the cellulose chains and is expressed as

$$DS = \left\lceil \frac{m + 2n + 3p}{AGUs_{TOT}} \right\rceil \tag{2}$$

For example, if we take into consideration 10 AGUs in total, for a DS of 0.7, we can expect 7 monosubstituted AGUs or, equivalently, 5 mono and 1 disubstituted AGUs. Kono *et al.* reported the exact molar ratio of each AGU in CMC with

Table 1. Signal Intensity Decay for the Carboxymethyl Substitutions in the Glucopyranose Unit of CMC with Different DS[a]

CMC (DS)	C1	CMC 2, 2,6 C2	CMC 2,3 C2	CMC 3, 6, 3,6 C2	CMC 3, 3,6 C3	CMC 2,3 C3	CMC 6, 2,6, 3,6 C6′	CMC 6, 2,6, 3,6 C6″	CMC 2, 3, 2,3 C6
0.7	0.89 (±0.11)	0.77 (±0.26)	ns[b]	0.82 (±0.28)	ns[b]	ns[b]	0.81 (±0.11)	0.56 (±0.17)	0.80 (±0.22)
0.9	0.60 (±0.10)	0.77 (±0.14)	ns[b]	0.67 (±0.22)	ns[b]	ns[b]	0.45 (±0.21)	0.30 (±0.10)	0.74 (±0.14)
1.2	0.68 (±0.08)	0.79 (±0.25)	ns[b]	0.62 (±0.31)	ns[b]	ns[b]	0.17 (±0.11)	0.43 (±0.12)	0.75 (±0.09)

[a]Signal intensity decay expressed as the ratio between the signal intensities recorded for a solution CMC 1% w/v in the presence and in the absence of 5 mM Fe^{3+} ions. [b]ns = no signal.

different DS, calculated by means of integral analysis of quantitative ^{13}C 1D solution-state NMR spectroscopy.[43]

Importantly, based on the DS of the CMCs used in our investigation, prevalence of monosubstituted AGUs was expected. However, even with the lowest investigated DS (0.7), the HSQC spectra showed unambiguous ^{13}C chemical shifts assigned to C2 and C3 of the 2,3-disubstituted AGU (for the full assigned HSQCs spectra, see Figure S1, Supporting Information). Based on this observation, we could not exclude the existence of the disubstituted species in solution.

Molecular Interaction of Fe^{3+} Ions with CMC. Paramagnetic NMR has been widely used for the structural characterization of metalloproteins,[44−46] for the introduction of paramagnetic restraints in drug discovery,[47] and, recently, to map protein−polymer conformations in bioconjugates.[48] Nonetheless, its application in soft-matter structural characterization is yet underexplored. We envisaged that the paramagnetic nature of Fe^{3+} metal ions could be used to achieve atomistic details on the CMC−Fe^{3+} ion interactions thanks to the distance-dependent paramagnetic contribution to NMR active nuclei relaxation.[49]

We recorded 2D $^1H-^{13}C$ HSQC NMR spectra of CMC 1% w/v dispersions with different DS in the absence and in the presence of Fe^{3+} ions (5 mM total molar concentration) and monitored signal decay induced by the metal ion−CMC carbon interactions. As shown in Figure 1, the HSQC spectra recorded in the presence of Fe^{3+} ions show complete signal disappearance for C2 and C3 of the 2,3-disubstituted CMC and C3 of the 3-mono and 3,6-disubstituted CMC. In addition, an intensity reduction for C6 signals of the 6-substituted CMC (6-mono, 2,6-di, and 3,6-disubstituted CMC) was observed. The observed differences indicate different spatial proximities between the distinct AGU units of CMC and the Fe^{3+} ions in the bound state.

Following a semiquantitative approach, which targets only CMC fast-relaxing components, the signal decay of each isolated peak in HSQC spectra was measured as the ratio of the average volumes between the samples in the presence and in the absence of Fe^{3+} ions. All the reported ratios show values equal or lower than one, indicating that for the investigated experimental conditions, the $^1H-^{13}C$ correlation peaks have about the same or a lower volume in the sample in the presence of Fe^{3+} ions (Table 1). Monitoring changes in the peaks' volume for different DS of CMC, we first noticed that the C2s of the 2- and 2,6- and of the 3-, 6-, and 3,6-substituted CMC show comparable signal reduction for each DS. On the contrary, the correlation peaks' volume for C1 and C6 of the 2-, 3-, and 2,3-substituted CMC does not show a significant reduction in the presence of Fe^{3+} ions for DS 0.7 but reveals a slight decrease for a higher DS. Strikingly, the signal corresponding to the carbon C6s of the 6-substituted CMC showed a halved or lower signal intensity for CMC with DS 0.9 and 1.2, while CMC with DS 0.7 retains *ca.* ~80% of the

original signal. Titration experiments performed for CMC DS 0.9 with increasing Fe^{3+} ion concentrations (Table S1) show a gradual decay for those carbons with lower interactions with the metal ions, while a significant signal intensity drop is reported for those nuclei in closer proximity with the metal center.

Overall, no drastic differences in the interaction mode between Fe^{3+} ions and CMC with increasing DS could be detected, but the Fe^{3+}−C6 contact enhanced for the CMC with DS 0.9 and 1.2. To interpret this result, we need to consider the nature of the CMC−Fe^{3+} interaction and the higher degree of covalency of the ligand−metal−σ bond (expressed by the nephelauxetic parameter, β) for CMC with DS 0.7 in comparison with DS 1.2.[50] Hence, for a comparable Fe^{3+} ion concentration in solution, in the case of CMC with the DS of 0.7, the Fe^{3+} ions remain, on the average, more anchored to the first interacting sites (*i.e.,* C2 and C3 of 2,3-disubstituted CMC and C3 of 3-substituted CMC). On the contrary, this interaction will have a more dynamic nature for CMC with a higher DS, resulting in the further contact of Fe^{3+} with the C6 binding site of the 6-substituted CMC.[50]

It is important to highlight that the used experimental conditions allow only for a partial recovery of the longitudinal magnetization, while a full recovery would occur with the use of longer relaxation delays. To test the influence of the used relaxation delay on the values obtained from the absolute peak-area ratio, we performed additional HSQC experiments with a relaxation delay of 21.5 s (Table S2). First, we observed the disappearance of the peaks belonging to C2 of the 2,3-disubstituted and C3 of the 3-mono, 2,3-di, and 3,6-disubstituted CMC, validating further the observations made with the experiments at a short relaxation delay. Interestingly, with HSQC experiments performed at a long relaxation delay, absolute ratio values higher than one were measured for C1 and C2, while comparable values with those reported in the short relaxation delay experiments were obtained for C6s (Tables 1 and S2). These data demonstrate that in the diamagnetic sample, the protons related to C1 and C2 do not fully recover their magnetization, while a complete recovery of magnetization with both short and long relaxation delays was proved for the protons in C6s. These results are not surprising as C6s (hexo-ring group) have higher mobility in comparison with the endo-ring, more fixed C1 and C2, reflecting into different relaxation properties of the ring protons.[51] In addition, it should be noted that CMC is a complex system with multiple dynamic regimes, some of which might require even longer times to completely relax. Indeed, the long-chain structure and high molecular weight of CMC result into a segmental motion rather than a classical isotropic tumbling in solution, with subsequent uneven spatial and temporal magnetic field variation in different portions of the sample.[52,53] Finally, the slight differences in absolute ratio values could be attributed to the different effect that PRE has on longitudinal
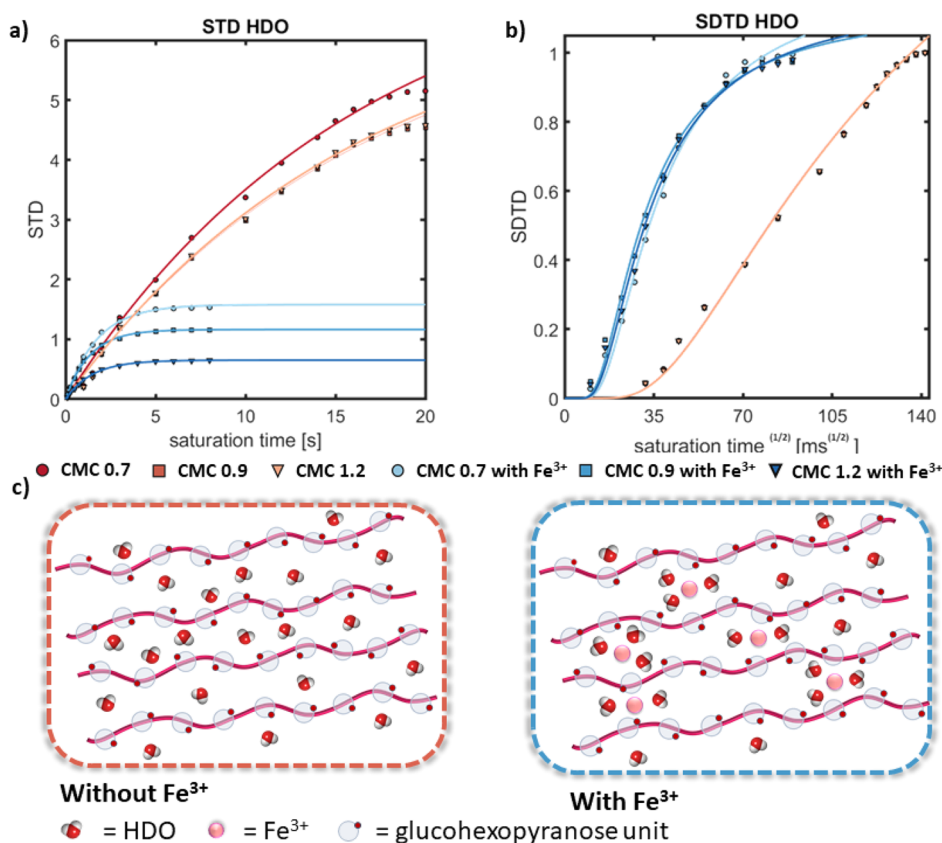
Figure 2. (a) STD build-up curves and (b) SDTD curves of the HDO peak for CMC 1% w/v with a DS of 0.7 (circles), 0.9 (squares), and 1.2 (triangles) in the absence (shades of red) and in the presence (shades of blue) of Fe^{3+} ions. (c) Schematic representation of water structuration before and upon introduction of Fe^{3+} ions.

and transverse relaxation mechanisms (T1 and T2) as reported by Clore and Iwahara, who deeply investigated the PRE effect in macromolecules.[54,55]

The Presence of Fe^{3+} Ions Induces Water Structuration in CMC. Localized interactions strongly influence the carbohydrate–water structure and dynamics. Carbohydrate–water interactions have a mutual behavior, with carbohydrates perturbing the structure of the surrounding water and, in turn, water affecting the structure of the solvated carbohydrate molecules. Importantly, carbohydrate–water interactions influence the macroscopic properties of different carbohydrates.[9]

STD NMR is a well-established technique for investigating the dynamic binding of small molecules with a low-to-medium binding affinity to proteins.[56] In soft matter, STD NMR has been used to study both gelator[8] and solvent molecules,[10,57] with recent application for elucidation of supramolecular protein–polymer interactions.[58]

To monitor the interaction of CMC 1% w/v dispersions with residually protonated water (HDO, present in solution following the exchange of one of the deuterium atoms of D_2O by a proton), we recorded a series of STD build-up curves with saturation time ranging from 1 to 20 s and from 0.1 to 8 s for CMC dispersions in the absence and in the presence of Fe^{3+} ions, respectively (Figures 2a and S2). For the samples in the absence of metal ions, the long saturation time required to reach the STD signal plateau for HDO is dictated by the long T1 relaxation time characteristic of large molecules that slowly tumble in solution. Importantly, the late-reaching plateau is indicative of the binding of HDO to the CMC network, as

water molecules free to tumble in solution normally have a T1 relaxation time of 2–3 s.[59] In the presence of Fe^{3+} ions, on the contrary, the paramagnetic effect of the metal determines a shortening of the relaxation time of HDO species, leading to a plateau at about 5 s saturation time.

The STD build-up curves show slower accumulation of magnetization in HDO for CMC samples in the absence of Fe^{3+} ions, as demonstrated by the smoother slopes of the STD build-up curves in comparison with the HDO STD build-up curves of the samples in the presence of Fe^{3+} metal ions (Figure 2a). These data indicate a more efficient magnetization transfer at the CMC–HDO interface for the samples in the presence of Fe^{3+} ions.

The faster accumulation of magnetization in the systems in the presence of Fe^{3+} ions might be correlated to a structuration of water molecules in the metal-coordinated system. To further confirm our observation, we applied the SDTD NMR methodology.[10] This methodology relies on the normalization of the STD factors, followed by fitting of the curves to the SDTD equation (eq 1, see Materials and Methods).

From the SDTD curves, changes in water structuration can be inferred by monitoring the initial part of the curves (lag phase), which corresponds to the minimum distance between the gelator and the solvent, and the slope of the curves, which corresponds to the rate of magnetization transfer from the gel network to the surrounding water, described as the spin diffusion coefficient (D_{SD}). The SDTD curves reveal no changes in water structuration for CMC in the absence of Fe^{3+} ions upon increasing the DS of CMC, as shown in Figure 2b, by the precise overlapping of the SDTD curves. Fitting of the
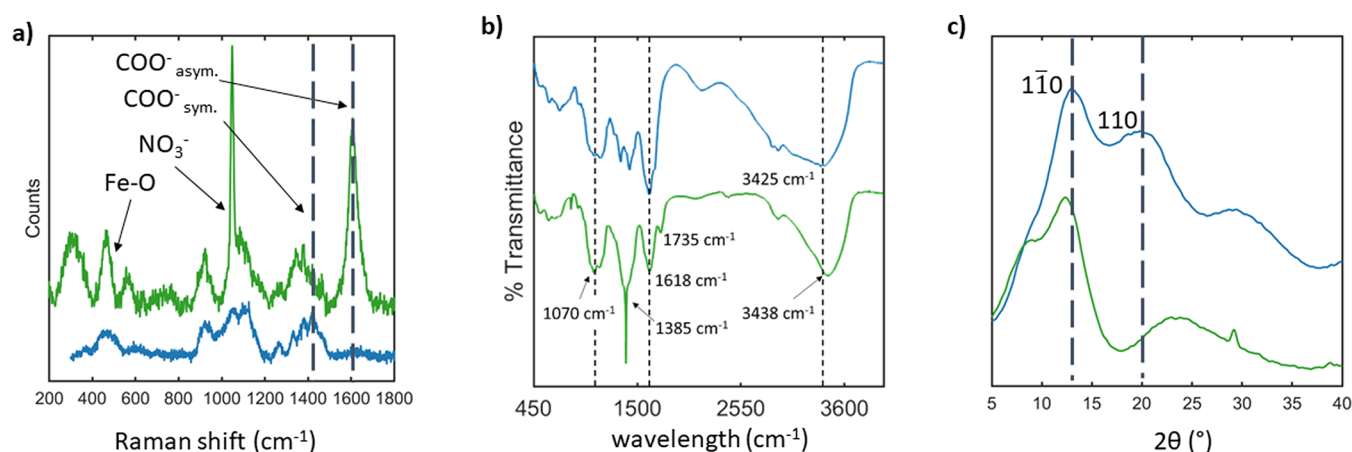
Figure 3. (a) Raman spectra, (b) FTIR spectra, and (c) PXRD patterns of the CMC (blue) and CMC−Fe^{3+} complex (green). CMC (DS 0.9) was formulated as CMC 4% w/v viscous dispersion and CMC 4% w/v cross-linked with $Fe(NO_3)_3$ 50 mM. All the samples were analyzed in solid form. Spectra have been offset on the ordinate for clarity.

curves resulted in the same spin diffusion coefficient (D_{SD}) for the three samples (Tables S3−S5). Visual inspection of the SDTD curves clearly shows a preferential binding of HDO to CMC upon introduction of Fe^{3+} ions, as expressed by the much faster growth of the SDTD build-up curves and the higher D_{SD} coefficient of HDO compared with the sample in the absence of Fe^{3+} ions (Figure 2b and Tables S3−S5). The faster SDTD build-up curve indicates that the degree of structuration of water in CMC increases upon introduction of Fe^{3+} ions (Figure 2c). Importantly, previous thermal analysis studies on CMC alone and in the complex with Fe^{3+} ions showed the presence of coordinated water for the metal-coordinated CMC.[50] Specifically, the increased structuration of water upon Fe^{3+} introduction observed by the SDTD NMR methodology might be attributed to (i) the formation of a denser network of water that shields the Fe^{3+} charge, (ii) the ion-induced chain association and chain−chain overlap with consequent water confinement, and (iii) structuration of water around the Na^+ ions bound to the chains. However, considering the stoichiometric concentration of Na^+ ions in the studied systems, a lower contribution to water structuration is expected for such species.

Coordination between the Carboxylic Units of CMC and the Fe^{3+} Ions. To further characterize the CMC−Fe^{3+} complexes, we used Raman scattering and FTIR spectroscopy. A complete assignment of CMC vibrational peaks is reported in Table S6, Supporting Information. Raman spectra of CMC in the absence and in the presence of Fe^{3+} ions are shown in Figure 3a. The spectra show a significant enhancement of the intensity of the band at ~1600 cm$^{−1}$ corresponding to the asymmetric stretching of the CMC carboxylate group in the presence of Fe^{3+} ions in comparison with CMC alone. It seems reasonable to assume that such modification of the Raman intensity may arise from the change in polarizability of the $COO^−$ moiety as a result of its interaction with the charged iron atom. We can therefore infer that the carboxymethyl group is involved in the coordination and in the O−Fe bond formed in the CMC−Fe^{3+} complex, although we cannot exclude that also intrachain or interchain hydrogen bonds could play a role in the spectral region around 1600 cm$^{−1}$.

FTIR spectra (Figure 3b) show a shift to a higher wavenumber of the band corresponding to bonded OH groups, from 3425 to 3438 cm$^{−1}$ for CMC in the absence and

in the presence of Fe^{3+} ions, respectively; we attributed this shift to a change of hydrogen bonds during complex formation and to the presence of coordinating water molecules.[60] In addition, the FTIR spectrum of CMC−Fe^{3+} complexes shows the vibration of the $NO_3^−$ ions at 1385 cm$^{−1}$ and the carbonyl absorption band at ca. ~1735 cm$^{−1}$, indicative of the presence of monodentate binding of the Fe^{3+} cation under the investigated conditions.[17]

Long-Range Ordering of CMC−Fe^{3+} Hydrogel. The structural long-range order of CMC in the absence and in the presence of Fe^{3+} ions has been characterized using the PXRD technique (Figure 3c). Both the PXRD diffraction patterns of the CMC and CMC−Fe^{3+} complex show broad peaks, indicating a major contribution of amorphous components and a low degree of crystallinity. Interestingly, for CMC alone, broad diffraction peaks at ca. ~2θ = 12.8 and 20° (d-spacing of 0.69 and 0.44 nm, respectively) could be identified. This diffraction pattern could resemble the cellulose type II arrangement, characterized by diffraction peaks located at ca. ~2θ = 12, 20, and 23° (d-spacing of 0.74, 0.44, and 0.39 nm, respectively) representing ($1\bar{1}0$), (110), and (020) planes.[61] Interestingly, the CMC−Fe^{3+} system shows a different diffraction pattern in comparison with CMC alone, indicating a different long-range organization of the two systems.

Modeling of CMC−Fe^{3+} Interaction. MD simulations were performed to achieve a more detailed understanding on the structure, dynamics, and physicochemical properties in the aqueous environment of our metal-coordinated hydrogel.[9,62]

To gain further insights into the glucopyranose sugar ring-Fe^{3+} interaction and the hydrogen bond cooperativity within adjacent glucopyranose rings in explicit water, we have focused on minimal systems made of β-1,4 trisaccharides with either mono or disubstitutions introduced at the central-ring level, with the position of the substitution indicated as primed numbers. In particular, to model the ability of Fe^{3+} ions to establish intra-ring interactions with disubstituted AGUs (with two carboxymethyl groups linked to the same hexopyranose ring), we introduced 2′,3′-di, 2′,6′-di, and 3′,6′-disubstitutions at the central ring of the β-1,4 trisaccharide (Figure S3a). To understand the formation of inter-residue interactions, instead, we have chosen to model three β-1,4 trisaccharides (D-cellotriose) with a single substitution introduced at the central-ring level of each chain (Figure S3b). The monosubstituted D-
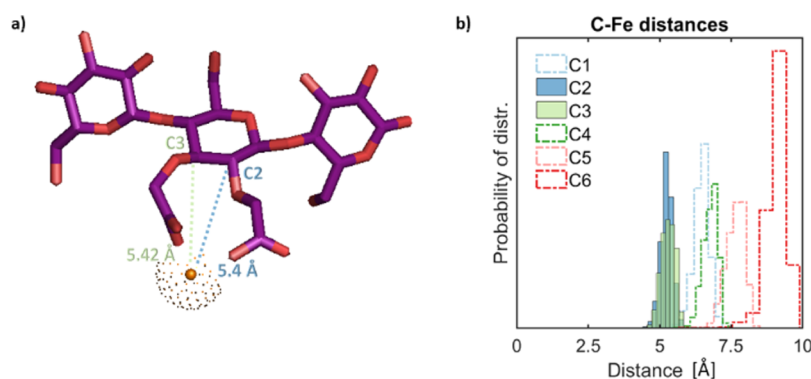
Figure 4. (a) MD frame showing Fe^{3+} bridging the carboxymethyl groups in 2′,3′-carboxymethyl cellotriose. The 2′,3′-carboxymethyl-cellotriose is represented as sticks, while the Fe^{3+} ion is represented as a dotted sphere; the structure has been extracted from VMD and then represented using Pymol. Distances between the Fe^{3+} ion and C2 and C3 of the 2′,3′-carboxymethyl-cellotriose central ring are reported. (b) Histograms of the distance between the Fe^{3+} ion and the carbons of the central ring of 2′,3′-carboxymethyl-cellotriose. The histograms for C1, C4, C5, and C6 are represented as stairs, while those for C2 and C3 are represented as bars.

carboxymethyl-cellotrioses are referred to as 2′-mono, 3′-mono, and 6′-mono. The following six systems were constructed: (i) 2′-mono/2′-mono, (ii) 2′-mono/3′mono, (iii) 3′-mono/3′-mono, (iv) 2′-mono/6′-mono, (v) 3′-mono/6′-mono, and (vi) 6′-mono/6′-mono. For the 2′-mono/2′-mono, 3′-mono/3′-mono, and the 6′-mono/6′-mono, we will refer to chain A and chain B to distinguish between the two different chains. For all the reported trajectories, the distribution of dihedral angles at the interglycosidic linkage level (Φ and Ψ angles) is in the energetically allowed region for β-1,4 saccharides (Figures S4 and S5), as reported by GlycoMapsDB (Glycosciences.de).[63]

Molecular Models of Intra-ring CMC−Fe^{3+} Ion Interaction-Disubstituted CMC Rings. For the single-chain disubstituted systems, analysis of the trajectories was performed in terms of the formation of an intra-ring $Fe^{3+}−COO^-$ bridge and of the distances between the carbons in the central ring and the Fe^{3+} ion. The structures of the final stages of the trajectory evolution are represented in Figure S6, Supporting Information.

For the 2′,3′-carboxymethyl cellotriose system, the trajectories show that the Fe^{3+} ion is located between the two carboxymethyl groups establishing an intra-ring connection (Figure 4a). From our trajectories, it is evident that the metal center is closer to C2 and C3 (*ca.* 5 Å distance) and farther from the other carbon nuclei (Figure 4b and Table S7). This result agrees well with our NMR data that show reduction of the signal intensities for C2 and C3 of the 2,3-disubstituted AGUs with the introduction of the metal center. In the case of the 2′,6′-disubstituted system, the establishment of the intra-ring connection between the Fe^{3+} ion and the carboxymethyl groups was followed by a conformational distortion of the hexopyranose ring from the $^4C_1$ chair conformation to the $^2S_0$ skew-boat conformation (Figure S6b). In this geometry, the Fe^{3+} ion is closer to C2 than to C6 (Figure S7 and Table S8), in disagreement with our HSQC spectra which show no significant intensity reduction for the C2 peak assigned to CMC 2-mono and 2,6-disubstitutions (*cf.* with Table 1). To prevent this ring-flip, which seems to be an artefact, we introduced a dihedral restraint (see Materials and Methods).[37] In this case, the Fe^{3+} ion remained anchored to the carboxyl group linked to C3. For the 3′,6′-disubstituted system, two different simulations with the Fe^{3+} ion located near the carboxylic group in C3 and C6 were run (Figure S6d,e). In

both situations, the Fe^{3+} ion remained anchored to a single carbonyl group, and no formation of a bridge between the Fe^{3+} ions and the two substituent groups was observed.

Molecular Models of Inter-chain CMC−Fe^{3+} Interaction-Ion-Induced Association of Two Monosubstituted Residues. For the six possible pairs of chains, with each chain monosubstituted either at the C2, C3, or C6 position in the central ring, we observed that the Fe^{3+} bridge between the two carboxylate groups persists throughout the simulations. Hence, we analyzed the trajectories in terms of the C−Fe^{3+} distances, the relative chain orientation, the presence of intra-/inter-chain hydrogen bonds, and the water radial distribution function (RDF). The final configurations of the trajectory evolution are reported in Figure S8.

We first measured the distances between the C2-, C3-, and C6-substituted carbons of the central ring and the Fe^{3+} ion for each one of the constructed models (Figure S9). The C2- and C6-substituted carbons show closer proximity to the Fe^{3+} metal center (between 4 and 6 Å) for the 2′-mono/6′-mono system (Figure S9a,b). For the 3′-mono/6′-mono and the 6′-mono/6′-mono systems, on the contrary, distances between *ca.* ∼6−8 Å were observed for C6−Fe^{3+} (Figure S9a), while the 2′-mono/2′-mono and 2′-mono/3′-mono system showed C2−Fe^{3+} distances in the range of 5−7 Å (Figure S9b). The C3-substituted systems (3′-mono/3′-mono, 2′-mono/3′-mono, and 3′-mono/6′-mono) showed C3−Fe^{3+} distances between 5 and 7 Å (Figure S9c). Generally, the distances between Fe^{3+} and C2, C3, or C6 carbons show minor differences from one system to another. Nonetheless, we highlight the difference on the C6−Fe^{3+} distance for the 2′-mono/6′-mono system in comparison with the 3′-mono/6′-mono and the 6′-mono/6′-mono systems. Considering our HSQC data, which show a closer proximity between the C6 of the 6-substituted AGUs and the Fe^{3+} ions, we can propose this as the leading contact at the initial stages of gelation.

Despite the persistence of the Fe^{3+}−oxo bridges, trimers are not frozen in a pair configuration but can change their relative position and orientation along the trajectories (a summary of initial condition and system evolution is reported in Table S9). In order to follow the relative orientation and alignment of the two chains in more detail, we constructed a dihedral (α), defined as the angle connecting chain A to chain B though the following atoms: O4, nr chain A → O1, r chain A → O1, r chain B → O4, nr chain B, were nr and r indicate the non-
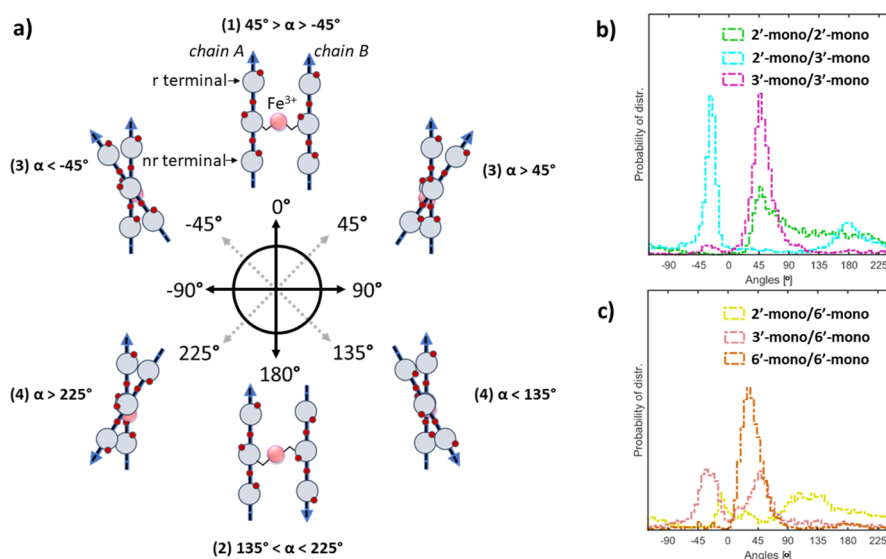
Figure 5. (a) Sketch of the relative orientation and alignment of a pair of trisaccharides expressed by the dihedral angle α. (b) Probability distribution of the dihedral angle α for the 2′-mono/2′-mono (blue), 2′-mono/3′-mono (green), and 3′-mono/3′-mono (red) systems. (c) Probability of distribution of the dihedral angle α for the 2′-mono/6′-mono (blue), 3′-mono/6′-mono (green), and 6′-mono/6′-mono (red) systems.

reducing and reducing ring terminals, respectively (Figure 5a). A schematic representation of the possible orientation (parallel or orthogonal) and alignment (polar or antipolar, in reference to the non-reducing and the reducing ring terminals for each chain) of the two chains is reported in Figure 5a. Angles in the ranges $-45° \leq \alpha \leq 45°$ and $135° \leq \alpha \leq 225°$ roughly correspond to chains in a parallel orientation with polar and antipolar alignment, respectively; intermediate values denote an orthogonal orientation. The probability distribution and the time evolution of the α angle for each system are shown in Figures 5b,c and S10, respectively.

Regardless of the starting orientation and alignment, all the investigated systems show a tendency to an approximately parallel orientation with polar alignment, with the only exception of the 2′-mono/2′-mono pair which also assumes a parallel orientation with antipolar alignment. These data could be indicative that even for a mostly amorphous system such as CMC (cf. Figure 3c), the connections driven by the cross-linker in the junction zones are characterized by a local structural alignment of the interacting interfaces. With the intent to correlate the chain orientation and alignment with the contacts in the junction zones of chains, we analyzed the formation of intra- and inter-chain hydrogen bonds. In our analysis, we excluded the hydroxyl groups in position C1 and C4 of the reducing and non-reducing terminals, respectively, as those characteristic chemical entities are not relevant for longer chains. Only hydrogen bonds presenting at least a 5% occurrence throughout the trajectories were considered. The following standard criteria for identification of hydrogen bonds were used: (i) an A–H distance of maximum 3.5 Å and (ii) an H–D–A bond angle (i.e., H–O⋯O) lower than 30°.[64] A full list of the most relevant inter-chain hydrogen bonds established by each system is reported in the Supporting Information, from Tables S10 to S13. The high mobility of the 2′-mono/2′-mono and the 3′-mono/6′-mono systems (cf. Figures 5 and S10a,e) is associated with the lack of hydrogen bonds with a high occurrence. In the 3′-mono/3′-mono and the 6′-mono/6′-mono systems, the two chains assume a preferential orthogonal orientation (cf. Figures 5 and S10c,f),

while in the 2′-mono/3′-mono and the 2′-mono/6′-mono systems, the two chains show a parallel orientation and swing between a polar and antipolar alignment (cf. Figures 5 and S10b,d).

Interestingly, for all the reported systems, the carboxymethyl group does not exclusively connect the two chains through the Fe^{3+} ions but actively interacts with the available hydroxyls of the adjacent chain. These models are in agreement with the results obtained from the FTIR spectrum of CMC–Fe^{3+} complexes, where the appearance of the absorption band at ca. ~1735 cm^{-1} supports the existence of carbonyls able to act as hydrogen-bond acceptors. The engagement of the carboxylate group in additional hydrogen bonds within the same residue and with adjacent residues in the same chain was already been reported by Yu et al. for short β-(1,4)-oligomers with the carboxymethyl substituent in position 3.[37] In here, we report for the first time the active role played by the carboxylate in interchain connections, even in the presence of a cross-linker.

In addition, analysis of the intrachain hydrogen bonds between the ring oxygen (O5) of one glucopyranose unit and the hydroxyl group in position 3 (HO3) of the adjacent unit (responsible for the stabilization of the cellobiose repeating unit) unveiled the preservation of this contact for all the reported systems (Table S14). On the contrary, the weaker intramolecular interaction between the hydroxyl in position 2 and the hydroxyl in position 6 of the adjacent ring shows a stronger perturbation, which results in the complete loss of this contact (Table S14).

Finally, we characterized the CMC–Fe^{3+}–water interactions at the molecular level by the RDFs. The RDFs of water oxygen and the Fe^{3+} ion for each of the investigated systems are shown in Figure 6. The pair distributions obtained display a well-defined first hydration shell with a density peak at ca. ~2 Å (Figure 6a), and its integral indicates a coordination number between two and four (Figure 6b). Visual analysis of the Fe^{3+}⋯OW distance evolution shows that the water molecules around the Fe^{3+} ion remain anchored throughout the trajectories, while the water molecules surrounding the sugar chain diffuse.
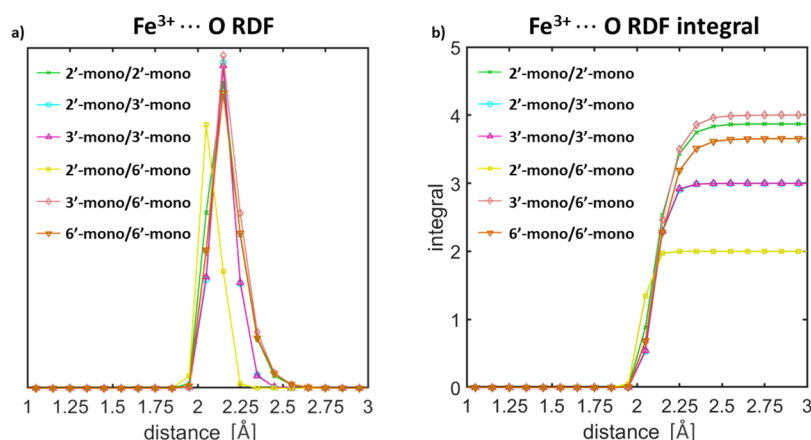
Figure 6. (a) RDF of water oxygens and Fe^{3+} ions and (b) its integral for the 2′-mono/2′-mono (green with a cross-marker), 2′-mono/3′-mono (light blue with a circle marker), 3′-mono/3′-mono (purple with an upward triangle marker), 2′-mono/6′-mono (yellow with a square marker), 3′-mono/6′-mono (pink with a diamond marker), and 6′-mono/6′-mono (orange with a downward triangle marker) systems.

Based on this model, we could attribute the increased water structuration upon Fe^{3+} introduction, experimentally observed by SDTD NMR spectroscopy, to the formation of a network of water molecules around the cross-linked Fe^{3+} ions.

CONCLUSIONS

In summary, insights into the structural basis for gelation of biopolymers coordinated by transition metals have been achieved using spectroscopic techniques and MD simulations. We demonstrated herein, for the first time, the application of an NMR approach based on the distance-dependent PRE property of paramagnetic transition metals to achieve atomistic details of the interaction between the metal ions and gelator network. Based on our HSQC data, we unveiled that the Fe^{3+} ions do not interact unselectively with the carboxyl groups present on the CMC surface. Indeed, the Fe^{3+} ions appear to preferentially establish at first an intra-ring connection with the 2,3-disubstituted CMC units. On the contrary, there is no indication of such interaction for the 2,6- and the 3,6-disubstituted units, which can be ascribed to the geometry of the systems. By employing Raman and FTIR spectroscopies, we have demonstrated the direct involvement of the carboxyl and hydroxyl groups on the polymer chain in the interaction with the Fe^{3+} ions. Molecular models of the CMC−Fe^{3+} interaction revealed the persistence of the Fe^{3+} ion inter-residue bridges between carboxylates linked to any position of the carboxymethyl monosubstituted D-cellotriose chains. This observation is of special interest for the understanding of the gelation process driven by Fe^{3+} ions in CMC, as it demonstrates that carboxymethyl groups in each position can equally contribute to the formation of inter-residue and inter-chain connections. The metal-induced chain association during the hydrogel formation not only preserves the intra-chain hydrogen bond network but also directs the establishment of inter-residue interactions in which the carbonyl units of the carboxymethyl substitutions are actively involved as hydrogen-bond acceptors when interacting with the Fe^{3+} ions with a monodentate binding mode. Remarkably, the combination of NMR spectroscopy and MD unveiled a solvent structuration around the metal cross-linkers, indicative of the active role played by the solvent in the hydrogel formation.

Metallo-supramolecular gels offer a facile route for the formulation of smart soft materials. In particular, the rational manipulation of their properties can be achieved with an appropriate understanding of the effects that the ligand structure, metal ion composition, metal−ligand interactions, solvent, and counterion have on the self-assembly process and on the consequent material behavior. Continued progress in the understanding of metal-coordinated hydrogels requires further exploration at all length scales and timescales in order to transform unique metal−ligand interactions into bulk smart-material properties.

ASSOCIATED CONTENT

ⓈSupporting Information

The Supporting Information is available free of charge at https://pubs.acs.org/doi/10.1021/acs.macromol.1c01756.

> ^{13}C HSQC spectra, STD NMR characterization, detailed assignment of Raman spectra, and modeling of the CMC−Fe^{3+} interaction (PDF)

AUTHOR INFORMATION

Corresponding Author

Marco Frasconi − *Department of Chemical Sciences, University of Padova, 35131 Padova, Italy;* ⓄRCID orcid.org/0000-0003-2010-175X; Email: marco.frasconi@unipd.it

Authors

Valeria Gabrielli − *Department of Chemical Sciences, University of Padova, 35131 Padova, Italy*

Roberto Baretta − *Department of Chemical Sciences, University of Padova, 35131 Padova, Italy*

Roberto Pilot − *Department of Chemical Sciences, University of Padova, 35131 Padova, Italy; Consorzio INSTM, I-50121 Firenze, Italy;* ⓄRCID orcid.org/0000-0001-6263-420X

Alberta Ferrarini − *Department of Chemical Sciences, University of Padova, 35131 Padova, Italy;* ⓄRCID orcid.org/0000-0001-6211-7202

Complete contact information is available at:
https://pubs.acs.org/10.1021/acs.macromol.1c01756

Notes

The authors declare no competing financial interest.

■ REFERENCES

(1) Khare, E.; Holten-Andersen, N.; Buehler, M. J. Transition-metal coordinate bonds for bioinspired macromolecules with tunable mechanical properties. *Nat. Rev. Mater.* **2021**, *6*, 421−436.

(2) Weng, W.; Beck, J. B.; Jamieson, A. M.; Rowan, S. J. Understanding the Mechanism of Gelation and Stimuli-Responsive Nature of a Class of Metallo-Supramolecular Gels. *J. Am. Chem. Soc.* **2006**, *128*, 11663−11672.

(3) Grindy, S. C.; Learsch, R.; Mozhdehi, D.; Cheng, J.; Barrett, D. G.; Guan, Z.; Messersmith, P. B.; Holten-Andersen, N. Control of hierarchical polymer mechanics with bioinspired metal-coordination dynamics. *Nat. Mater.* **2015**, *14*, 1210−1216.

(4) Li, C.-H.; Wang, C.; Keplinger, C.; Zuo, J.-L.; Jin, L.; Sun, Y.; Zheng, P.; Cao, Y.; Lissel, F.; Linder, C.; You, X.-Z.; Bao, Z. A highly stretchable autonomous self-healing elastomer. *Nat. Chem.* **2016**, *8*, 618−624.

(5) Sun, W.; Xue, B.; Fan, Q.; Tao, R.; Wang, C.; Wang, X.; Li, Y.; Qin, M.; Wang, W.; Chen, B.; Cao, Y. Molecular engineering of metal coordination interactions for strong, tough, and fast-recovery hydrogels. *Sci. Adv.* **2020**, *6*, No. eaaz9531.

(6) Yang, H.; Ghiassinejad, S.; Van Ruymbeke, E.; Fustin, C.-A. Tunable Interpenetrating Polymer Network Hydrogels Based on Dynamic Covalent Bonds and Metal−Ligand Bonds. *Macromolecules* **2020**, *53*, 6956−6967.

(7) Ahmadi, M.; Seiffert, S. Coordination Geometry Preference Regulates the Structure and Dynamics of Metallo-Supramolecular Polymer Networks. *Macromolecules* **2021**, *54*, 1388−1400.

(8) Ramalhete, S. M.; Nartowski, K. P.; Sarathchandra, N.; Foster, J. S.; Round, A. N.; Angulo, J.; Lloyd, G. O.; Khimyak, Y. Z. Supramolecular Amino Acid Based Hydrogels: Probing the Contribution of Additive Molecules using NMR Spectroscopy. *Chem.—Eur. J.* **2017**, *23*, 8014−8024.

(9) Corzana, F.; Motawia, M. S.; Du Penhoat, C. H.; Perez, S.; Tschampel, S. M.; Woods, R. J.; Engelsen, S. B. A hydration study of (1→4) and (1→6) linked α-glucans by comparative 10 ns molecular dynamics simulations and 500-MHz NMR. *J. Comput. Chem.* **2004**, *25*, 573−586.

(10) Gabrielli, V.; Kuraite, A.; Da Silva, M. A.; Edler, K. J.; Angulo, J.; Nepravishta, R.; Muñoz-García, J. C.; Khimyak, Y. Z. Spin diffusion transfer difference (SDTD) NMR: An advanced method for the characterisation of water structuration within particle networks. *J. Colloid Interface Sci.* **2021**, *594*, 217−227.

(11) Ajdary, R.; Tardy, B. L.; Mattos, B. D.; Bai, L.; Rojas, O. J. Plant Nanomaterials and Inspiration from Nature: Water Interactions and Hierarchically Structured Hydrogels. *Adv. Mater.* **2021**, *33*, 2001085.

(12) Pérez, S.; Samain, D. Structure and Engineering of Celluloses. *Adv. Carbohydr. Chem. Biochem.* **2010**, *64*, 25−116.

(13) Zennifer, A.; Senthilvelan, P.; Sethuraman, S.; Sundaramurthi, D. Key advances of carboxymethyl cellulose in tissue engineering & 3D bioprinting applications. *Carbohydr. Polym.* **2021**, *256*, 117561.

(14) Lopez, C. G.; Colby, R. H.; Graham, P.; Cabral, J. T. Viscosity and Scaling of Semiflexible Polyelectrolyte NaCMC in Aqueous Salt Solutions. *Macromolecules* **2017**, *50*, 332−338.

(15) Sharratt, W. N.; O'Connell, R.; Rogers, S. E.; Lopez, C. G.; Cabral, J. T. Conformation and Phase Behavior of Sodium Carboxymethyl Cellulose in the Presence of Mono- and Divalent Salts. *Macromolecules* **2020**, *53*, 1451−1463.

(16) Guo, Z.; Zhang, D.; Song, S.; Shu, Y.; Chen, X.; Wang, J. Complexes of magnetic nanospheres with amphiprotic polymer−Zn systems for the selective isolation of lactoferrin. *J. Mater. Chem. B* **2018**, *6*, 5596−5603.

(17) Sharratt, W. N.; Lopez, C. G.; Sarkis, M.; Tyagi, G.; O'Connell, R.; Rogers, S. E.; Cabral, J. T. Ionotropic Gelation Fronts in Sodium Carboxymethyl Cellulose for Hydrogel Particle Formation. *Gels* **2021**, *7*, 44.

(18) Auletta, J. T.; Ledonne, G. J.; Gronborg, K. C.; Ladd, C. D.; Liu, H.; Clark, W. W.; Meyer, T. Y. Stimuli-Responsive Iron-Cross-Linked Hydrogels That Undergo Redox-Driven Switching between Hard and Soft States. *Macromolecules* **2015**, *48*, 1736−1747.

(19) Fadeev, M.; Davidson-Rozenfeld, G.; Biniuri, Y.; Yakobi, R.; Cazelles, R.; Aleman-Garcia, M. A.; Willner, I. Redox-triggered hydrogels revealing switchable stiffness properties and shape-memory functions. *Polym. Chem.* **2018**, *9*, 2905−2912.

(20) Jin, Z.; Güven, G.; Bocharova, V.; Halámek, J.; Tokarev, I.; Minko, S.; Melman, A.; Mandler, D.; Katz, E. Electrochemically Controlled Drug-Mimicking Protein Release from Iron-Alginate Thin-Films Associated with an Electrode. *ACS Appl. Mater. Interfaces* **2012**, *4*, 466−475.

(21) Narayanan, R. P.; Melman, G.; Letourneau, N. J.; Mendelson, N. L.; Melman, A. Photodegradable Iron(III) Cross-Linked Alginate Gels. *Biomacromolecules* **2012**, *13*, 2465−2471.

(22) Giammanco, G. E.; Sosnofsky, C. T.; Ostrowski, A. D. Light-Responsive Iron(III)−Polysaccharide Coordination Hydrogels for Controlled Delivery. *ACS Appl. Mater. Interfaces* **2015**, *7*, 3068−3076.

(23) Li, H.; Wang, H.; Zhang, D.; Xu, Z.; Liu, W. A highly tough and stiff supramolecular polymer double network hydrogel. *Polymer* **2018**, *153*, 193−200.

(24) Bouguet-Bonnet, S.; Yemloul, M.; Canet, D. New application of proton nuclear spin relaxation unraveling the intermolecular structural features of low-molecular-weight organogel fibers. *J. Am. Chem. Soc.* **2012**, *134*, 10621−10627.

(25) Lozano, V.; Hernández, R.; Ardá, A.; Jiménez-Barbero, J.; Mijangos, C.; Pérez-Pérez, M.-J. An asparagine/tryptophan organogel showing a selective response towards fluoride anions. *J. Mater. Chem.* **2011**, *21*, 8862.

(26) Kumashiro, K. K.; Schmidt-Rohr, K.; Murphy, O. J.; Ouellette, K. L.; Cramer, W. A.; Thompson, L. K. A Novel Tool for Probing Membrane Protein Structure: Solid-State NMR with Proton Spin Diffusion and X-Nucleus Detection. *J. Am. Chem. Soc.* **1998**, *120*, 5043−5051.

(27) Group, W. *GLYCAM Web*.

(28) *Schrödinger Release: 2021-2*; Maestro, Schrödinger: New York, NY, 2021.

(29) Case, D. A.; Belfon, K.; Ben-Shalom, I. Y.; Brozell, S. R.; Cerutti, D. S.; Cheatham, T. E., III; Cruzeiro, V. W. D.; Darden, T. A.; Duke, R. E.; Giambasu, G.; Gilson, M. K.; Gohlke, H.; Goetz, A. W.; Harris, R.; Izadi, S.; Izmailov, S. A.; Jin, C.; Kasavajhala, K.; Kaymak, M. C.; King, E.; Kovalenko, A.; Kurtzman, T.; Lee, T. S.; LeGrand, S.; Li, P.; Lin, C.; Liu, J.; Luchko, T.; Luo, R.; Machado, M.; Man, V.; Manathunga, M.; Merz, K. M.; Miao, Y.; Mikhailovskii, O.; Monard, G.; Nguyen, H.; O'Hearn, K. A.; Onufriev, A.; Pan, F.; Pantano, S.; Qi, R.; Rahnamoun, A.; Roe, D. R.; Roitberg, A.; Sagui, C.; Schott-Verdugo, S.; Shen, J.; Simmerling, C. L.; Skrynnikov, N. R.; Smith, J.; Swails, J.; Walker, R. C.; Wang, J.; Wei, H.; Wolf, R. M.; Wu, X.; Xue, Y.; York, D. M.; Zhao, S.; Kollman, P. A. *Amber 2021*; University of California: San Francisco, 2021.

(30) Kirschner, K. N.; Yongye, A. B.; Tschampel, S. M.; González-Outeiriño, J.; Daniels, C. R.; Foley, B. L.; Woods, R. J. GLYCAM06: A generalizable biomolecular force field. Carbohydrates. *J. Comput. Chem.* **2008**, *29*, 622−655.

(31) Li, P.; Song, L. F.; Merz, K. M. Parameterization of Highly Charged Metal Ions Using the 12-6-4 LJ-Type Nonbonded Model in Explicit Water. *J. Phys. Chem. B* **2015**, *119*, 883−895.

(32) Bernardi, A.; Faller, R.; Reith, D.; Kirschner, K. N. ACPYPE update for nonuniform 1−4 scale factors: Conversion of the GLYCAM06 force field from AMBER to GROMACS. *SoftwareX* **2019**, *10*, 100241.

(33) Bekker, H.; Berendsen, H. J. C.; Dijkstra, E. J.; Achterop, S.; van Drunen, R.; van der Spoel, D.; Sijbers, A.; Keegstra, H.; Renardus, M. K. R. Gromacs: A parallel computer for molecular dynamics simulations. *Phys. Comput.* **1993**, *92*, 252−256.

(34) Van Der Spoel, D.; Lindahl, E.; Hess, B.; Groenhof, G.; Mark, A. E.; Berendsen, H. J. C. GROMACS: Fast, flexible, and free. *J. Comput. Chem.* **2005**, *26*, 1701−1718.

(35) Darden, T.; York, D.; Pedersen, L. Particle mesh Ewald: AnN·log(N) method for Ewald sums in large systems. *J. Chem. Phys.* **1993**, *98*, 10089−10092.

(36) Hess, B.; Bekker, H.; Berendsen, H. J. C.; Fraaije, J. G. E. M. LINCS: A linear constraint solver for molecular simulations. *J. Comput. Chem.* **1997**, *18*, 1463−1472.

(37) Yu, Y.; Tyrikos-Ergas, T.; Zhu, Y.; Fittolani, G.; Bordoni, V.; Singhal, A.; Fair, R. J.; Grafmüller, A.; Seeberger, P. H.; Delbianco, M. Systematic Hydrogen-Bond Manipulations To Establish Polysaccharide Structure−Property Correlations. *Angew. Chem., Int. Ed.* **2019**, *131*, 13261−13266.

(38) Jiang, F.; Dallas, J. L.; Ahn, B. K.; Hsieh, Y.-L. 1D and 2D NMR of nanocellulose in aqueous colloidal suspensions. *Carbohydr. Polym.* **2014**, *110*, 360−366.

(39) Andrade, P.; Muñoz-García, J. C.; Pergolizzi, G.; Gabrielli, V.; Nepogodiev, S. A.; Iuga, D.; Fábián, L.; Nigmatullin, R.; Johns, M. A.; Harniman, R.; Eichhorn, S. J.; Angulo, J.; Khimyak, Y. Z.; Field, R. A. Chemoenzymatic Synthesis of Fluorinated Cellodextrins Identifies a New Allomorph for Cellulose-Like Materials. *Chem.−Eur. J.* **2021**, *27*, 1374−1382.

(40) Kono, H. 1H and 13C chemical shift assignment of the monomers that comprise carboxymethyl cellulose. *Carbohydr. Polym.* **2013**, *97*, 384−390.

(41) Schaefer, J. High-Resolution Pulsed Carbon-13 Nuclear Magnetic Resonance Analysis of Some Cross-Linked Polymers. *Macromolecules* **1971**, *4*, 110−112.

(42) Kono, H.; Anai, H.; Hashimoto, H.; Shimizu, Y. 13C-detection two-dimensional NMR approaches for cellulose derivatives. *Cellulose* **2015**, *22*, 2927−2942.

(43) Kono, H.; Oshima, K.; Hashimoto, H.; Shimizu, Y.; Tajima, K. NMR characterization of sodium carboxymethyl cellulose: Substituent distribution and mole fraction of monomers in the polymer chains. *Carbohydr. Polym.* **2016**, *146*, 1−9.

(44) Pell, A. J.; Pintacuda, G.; Grey, C. P. Paramagnetic NMR in solution and the solid state. *Prog. Nucl. Magn. Reson. Spectrosc.* **2019**, *111*, 1−271.

(45) Ravera, E.; Parigi, G.; Luchinat, C. What are the methodological and theoretical prospects for paramagnetic NMR in structural biology? A glimpse into the crystal ball. *J. Magn. Reson.* **2019**, *306*, 173−179.

(46) Unione, L.; Ortega, G.; Mallagaray, A.; Corzana, F.; Pérez-Castells, J.; Canales, A.; Jiménez-Barbero, J.; Millet, O. Unraveling the Conformational Landscape of Ligand Binding to Glucose/Galactose-Binding Protein by Paramagnetic NMR and MD Simulations. *ACS Chem. Biol.* **2016**, *11*, 2149−2157.

(47) Softley, C. A.; Bostock, M. J.; Popowicz, G. M.; Sattler, M. Paramagnetic NMR in drug discovery. *J. Biomol. NMR* **2020**, *74*, 287−309.

(48) Burridge, K. M.; Shurina, B. A.; Kozuszek, C. T.; Parnell, R. F.; Montgomery, J. S.; Vanpelt, J. L.; Daman, N. M.; McCarrick, R. M.; Ramelot, T. A.; Konkolewicz, D.; Page, R. C. Mapping protein−polymer conformations in bioconjugates with atomic precision. *Chem. Sci.* **2020**, *11*, 6160−6166.

(49) Bertini, I.; Luchinat, C.; Parigi, G.; Ravera, E. NMR of Paramagnetic Molecules. *Current Methods in Inorganic Chemistry II*; Elsevier Science, 2016.

(50) Basta, A. H.; El-Saied, H. Characterization of polymer complexes by thermal and IR spectral analyses. *Polym.-Plast. Technol. Eng.* **2000**, *39*, 887−904.

(51) Claridge, T. D. W. *High-Resolution NMR Techniques in Organic Chemistry*, 3rd ed.; Elsevier, 2016.

(52) Levitt, M. H., *Spin Dynamics: Basics of Nuclear Magnetic Resonance*, 2nd ed.; Wiley, 2008.

(53) Dais, P.; Perlin, A. S. Proton Spin-Lattice Relaxation Rates in the Structural Analysis of Carbohydrate Molecules in Solution. *Adv. Carbohydr. Chem. Biochem.* **1987**, *45*, 125−168.

(54) Iwahara, J.; Tang, C.; Marius Clore, G. Practical aspects of 1H transverse paramagnetic relaxation enhancement measurements on macromolecules. *J. Magn. Reson.* **2007**, *184*, 185−195.

(55) Iwahara, J.; Schwieters, C. D.; Clore, G. M. Ensemble Approach for NMR Structure Refinement against 1H Paramagnetic Relaxation Enhancement Data Arising from a Flexible Paramagnetic Group Attached to a Macromolecule. *J. Am. Chem. Soc.* **2004**, *126*, 5879−5896.

(56) Angulo, J.; Díaz, I.; Reina, J. J.; Tabarani, G.; Fieschi, F.; Rojo, J.; Nieto, P. M. Saturation Transfer Difference (STD) NMR Spectroscopy Characterization of Dual Binding Mode of a Mannose Disaccharide to DC-SIGN. *ChemBioChem* **2008**, *9*, 2225−2227.

(57) Calabrese, V.; Muñoz-García, J. C.; Schmitt, J.; da Silva, M. A.; Scott, J. L.; Angulo, J.; Khimyak, Y. Z.; Edler, K. J. Understanding heat driven gelation of anionic cellulose nanofibrils: Combining saturation transfer difference (STD) NMR, small angle X-ray scattering (SAXS) and rheology. *J. Colloid Interface Sci.* **2019**, *535*, 205−213.

(58) Xu, Y. D.; Lai, R. Y.; Procházková, E.; Stenzel, M. H. Saturation Transfer Difference NMR Spectroscopy for the Elucidation of Supramolecular Albumin−Polymer Interactions. *ACS Macro Lett.* **2021**, *10*, 819−824.

(59) Blinc, A.; Lahajnar, G.; Blinc, R.; Zidanš, A.; Sepe, A. Proton NMR study of the state of water in fibrin gels, plasma, and blood clots. *Magn. Reson. Med.* **1990**, *14*, 105−122.

(60) Hosny, W. M.; Basta, A. H.; El-Saied, H. Metal Chelates with Some Cellulose Derivatives: Synthesis and Characterization of Some Iron(III) Complexes with Cellulose Ethers. *Polym. Int.* **1997**, *42*, 157−162.

(61) Langan, P.; Nishiyama, Y.; Chanzy, H. X-ray Structure of Mercerized Cellulose II at 1 Å Resolution. *Biomacromolecules* **2001**, *2*, 410−416.

(62) Braccini, I.; Pérez, S. Molecular Basis of Ca^{2+}-Induced Gelation in Alginates and Pectins: The Egg-Box Model Revisited. *Biomacromolecules* **2001**, *2*, 1089−1096.

(63) Böhm, M.; Bohne-Lang, A.; Frank, M.; Loss, A.; Rojas-Macias, M. A.; Lütteke, T.; Glycosciences, D. B. an annotated data collection linking glycomics and proteomics data (2018 update). *Nucleic Acids Res.* **2019**, *47*, D1195−D1201.

(64) Luzar, A. Resolving the hydrogen bond dynamics conundrum. *J. Chem. Phys.* **2000**, *113*, 10663−10675.